Rapid Communications | Editors' Suggestion

High-density two-dimensional electron system induced by oxygen vacancies in ZnO

T. C. Rödel,[1,2,3] J. Dai,[1] F. Fortuna,[1] E. Frantzeskakis,[1] P. Le Fèvre,[2] F. Bertran,[2] M. Kobayashi,[4] R. Yukawa,[4] T. Mitsuhashi,[4] M. Kitamura,[4] K. Horiba,[4] H. Kumigashira,[4] and A. F. Santander-Syro[1,*]

[1]*CSNSM, Univ. Paris-Sud, CNRS/IN2P3, Université Paris-Saclay, 91405 Orsay Cedex, France*

[2]*Synchrotron SOLEIL, L'Orme des Merisiers, Saint-Aubin-BP48, 91192 Gif-sur-Yvette, France*

[3]*Laboratory for Photovoltaics, Physics and Material Science Research Unit, University of Luxembourg, L-4422 Belvaux, Luxembourg*

[4]*Photon Factory, Institute of Materials Structure Science, High Energy Accelerator Research Organization (KEK), 1-1 Oho, Tsukuba 305-0801, Japan*

(Received 18 February 2018; published 14 May 2018)

We realize a two-dimensional electron system (2DES) in ZnO by simply depositing pure aluminum on its surface in ultrahigh vacuum and characterize its electronic structure by using angle-resolved photoemission spectroscopy. The aluminum oxidizes into alumina by creating oxygen vacancies that dope the bulk conduction band of ZnO and confine the electrons near its surface. The electron density of the 2DES is up to two orders of magnitude higher than those obtained in ZnO heterostructures. The 2DES shows two *s*-type subbands, that we compare with the *d*-like 2DESs in titanates, with clear signatures of many-body interactions that we analyze through a self-consistent extraction of the system self-energy and a modeling as a coupling of a two-dimensional Fermi liquid with a Debye distribution of phonons.

DOI: 10.1103/PhysRevMaterials.2.051601

ZnO is a transparent, easy to fabricate oxide semiconductor with a direct band gap $E_g = 3.3$ eV. Its many uses include window layers in photovoltaic devices, varistors for voltage-surge protection, UV absorbers, gas sensors, and catalytic devices [1,2]. ZnO is also a candidate for novel applications, such as transparent field effect transistors, UV laser diodes, memristors, or high-temperature–high-field electronics [1–6]. In fact, ZnO can be seen as a link between the classical group-IV or -III-V semiconductors, e.g., Si or GaAs, and transition-metal oxides (TMOs), such as $SrTiO_3$. Due to their valence *d* orbitals, the latter show a rich variety of collective electronic phenomena, like magnetism or high-T_c superconductivity [7,8]. Moreover, the controlled fabrication of a two-dimensional electron system (2DES) in ZnO can result in extremely high electron mobilities, even competing with those of GaAs-based heterostructures, and showing the quantum Hall effects [9,10].

Two-dimensional electron systems (2DESs) in TMOs have also improved in mobility over the last decade, but what makes them really unique is the control of superconductivity, magnetism and spin-orbit coupling by varying the electron density using a gate voltage [11–22]. Additionally, for many insulating TMOs, recent works demonstrated that oxygen vacancies near the surface provide a simple and efficient mechanism to produce a 2DES, with electron densities as high as $n_{2D} \sim 3 \times 10^{14}$ cm^{-2} [23–33], and showing magnetic states linked to the presence of such vacancies [34].

Here we show, by using angle-resolved photoemission spectroscopy (ARPES), that the simple evaporation in ultrahigh vacuum (UHV) of an atomic layer of pure aluminum on ZnO creates a 2DES with electron densities up to two orders of magnitude higher than in previous studies. We demonstrate that the 2DES results from oxidation of the Al layer and concomitant doping with oxygen vacancies of the underlying ZnO surface. The 2DES is composed of two subbands with different effective masses, as the mass of the inner band is wholly renormalized due to the energetic proximity of its band bottom with a phonon frequency, whereas the outer band, dispersing deeper in energy, shows only a kink due to the electron-phonon interaction. We thoroughly investigate the electron-phonon coupling by a self-consistent extraction of the electron self-energy. We deduce an Eliashberg coupling function wholly compatible with a two-dimensional (2D) Debye-like distribution of phonons and a mass-enhancement parameter $\lambda = 0.3$.

Previous photoemission experiments on ZnO [35–40] showed that hydrogenation of its polar or nonpolar surfaces, for instance through chemisorption of hydrogen, methanol, or water, induces a downward band bending and the formation of a 2DES with a moderate electron density $n_{2D} \leqslant 2 \times 10^{13}$ cm^{-2}, showing only one broad shallow subband below the Fermi level (E_F) [39]. More recently, several ARPES studies focused on the many-body phenomena of electron-phonon coupling in oxides, demonstrating that, at *low carrier densities*, the 2DES in TiO_2, $SrTiO_3$, and also ZnO are composed of polarons [41–43]. Due to a nonadiabatic electron-phonon coupling, the polaronic regime changes to a Fermi-liquid behavior with increasing electron densities, as electronic screening of the polar lattice becomes more efficient [44]. However, the Fermi-liquid regime in ZnO has not been studied yet, as previous doping methods of the surface were insufficient to achieve high electron densities. Attaining large carrier densities for a 2DES in ZnO is also appealing for applications in high-power transparent electronics.

*andres.santander@csnsm.in2p3.fr

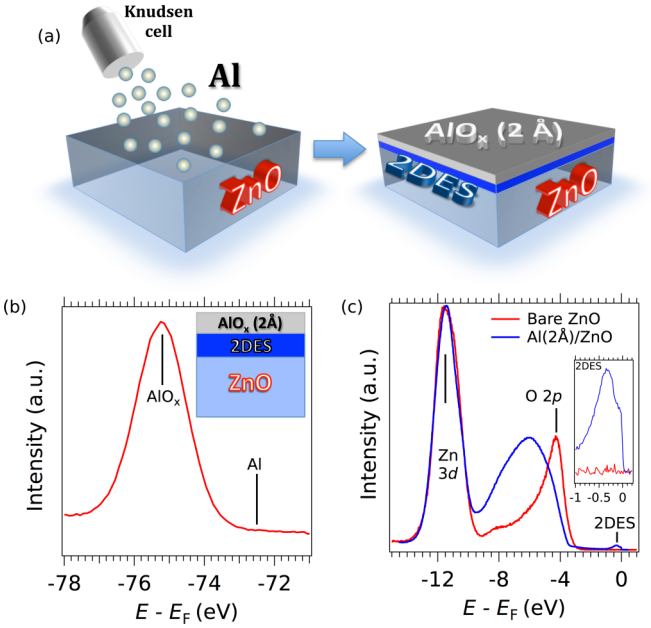

FIG. 1. (a) Schematics of the mechanism of formation of a highly doped 2DES in ZnO. Pure aluminum is thermally evaporated at room temperature in UHV at the surface of ZnO. The Al becomes alumina by pumping oxygen from the ZnO, hereby producing a 2DES at the AlO_x/ZnO interface. (b) Al $2p$ core level, measured right after deposition on ZnO. Its binding energy corresponds to *completely oxidized* aluminum (AlO_x), while no peak of pure aluminum is observed. The inset shows the AlO_x/ZnO interface and the 2DES obtained after deposition of Al on ZnO. (c) Comparison of the valence bands and near-E_F spectra of bare ZnO and Al-capped ZnO (red and blue curves, respectively). The surface redox reaction after Al deposition modifies the O $2p$ valence band and produces an intense quasiparticle peak at E_F, corresponding to the 2DES. As no Fermi level was detected on the spectrum at the bare ZnO surface, its binding energies were calibrated with respect to the Zn $3d$ peak of the AlO_x/ZnO interface. Photoemission data in this and all other figures of this paper were measured at $T = 7$ K.

We now discuss our main findings. Henceforth, we focus on data measured at the O-terminated ZnO(000$\bar{1}$) surface. As shown in the supplemental material [45], similar results are obtained at the ZnO(0001) (zinc-terminated) interface, although the resulting 2DES has a slightly smaller electron density. Furthermore, to recall that we deposited pure Al (not aluminum oxide) on the ZnO surface, we note the resulting AlO_x capping layer simply as "Al," specifying in parentheses the evaporated thickness. Additional details on the crystallographic nomenclature, surface preparation, aluminum evaporation, and ARPES measurements are provided in the supplemental material [45].

The creation of a 2DES by Al deposition is identical to the procedure described in Ref. [31] and is summarized in Fig. 1(a). We use thermal evaporation from a Knudsen cell to deposit, at room temperature in UHV, an atomically thin layer of Al on the ZnO surface. Due to an efficient redox reaction, the Al oxidizes into insulating AlO_x by pumping oxygen from the first atomic planes of the underlying ZnO. The oxygen vacancies dope the conduction band and create the potential that confines the electrons at the surface, resulting in multiple subbands due to the quantum confinement.

Figure 1(b) shows that the Al-$2p$ core-level peak at the Al(2 Å)/ZnO interface corresponds to oxidized aluminum, whose binding energy ($E - E_F = -75$ eV) is very different from the one of metallic aluminum (−72.5 eV) [31]. Figure 1(c) compares the valence-band of the bare, stoichiometric ZnO(000$\bar{1}$) surface (red curve) and of the Al(2 Å)/ZnO interface (blue curve). We observe that, contrary to oxygen-deficient surfaces or interfaces of TMOs [31,46], there are no measurable states corresponding to localized electrons (i.e., deep donors) in the band gap of oxygen-deficient ZnO. The absence of such states in ZnO emphasizes the simpler character of a 2DES based on s-valence electrons, compared with the d-valence electrons in TMOs. On the other hand, the binding energy and shape of the O $2p$ valence band are dramatically changed, possibly because the O-$2p$ valence band of the oxidized Al layer is at a binding energy of ≈6 eV.

It is worth noting that, for previously reported 2DES in oxides, an intense synchrotron beam can create oxygen vacancies due to desorption induced by electronic transitions [47]. This process, based on the photoexcitation of core levels, is different in titanates and ZnO [48]. In fact, as shown in the inset of Fig. 1(c), the bare ZnO surface does not show any states at the Fermi level when exposed to the strong synchrotron light used for our experiments. Only the Al capping creates such states at E_F, and they appear in the photoemission spectra instantly. Thus, our results demonstrate that the creation of 2DES in oxides using Al capping is a much more general mechanism, enabling furthermore ARPES studies independent from the relaxation mechanism of photoexcited core levels.

The contribution of oxygen vacancies to n-type conductivity in bulk ZnO has been a controversial issue [49–54]. The photoemission signatures observed here after Al deposition; namely, an oxidized Al core level and the appearance of a 2DES at E_F, are identical to those reported in other oxides [31], indicating that the mechanisms underlying the 2DES formation are similar. Future theoretical works should explore in detail the energetics and specific role of oxygen vacancies near the *surface* of ZnO.

We now characterize the electronic structure of the 2DES at the Al(2 Å)/ZnO(000$\bar{1}$) (oxygen-terminated) interface. Figure 2(a) shows the in-plane Fermi-surface map measured by ARPES. There are two metallic states forming concentric circular Fermi sheets around Γ, which correspond to confined states of ZnO's conduction band—which is formed by orbitals of s character. Figure 2(b) presents the energy-momentum dispersion map of the two states forming the above concentric Fermi circles, henceforth called outer (o) and inner (i) subbands. They were measured around the bulk Γ_{002} point along the in-plane $k_{\langle 11\bar{2}0\rangle}$ direction. Such 2DESs with two subbands in ZnO have not been observed before, as electron densities were not large enough in previous studies [36–40,43]. Additional data presented in the supplemental material [45] demonstrates that the in-plane periodicity of the electronic structure corresponds to the one of an unreconstructed surface, and that the two subbands form cylindrical, nondispersive Fermi surfaces along the (0001) direction perpendicular to the interface, confirming their 2D character.

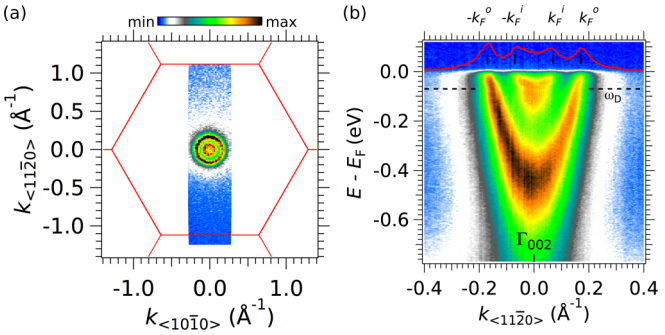

FIG. 2. (a) ARPES Fermi-surface map of the Al(2 Å)/ZnO interface in the O-terminated [000$\bar{1}$] plane, measured at $h\nu = 88$ eV with linear-horizontal light polarization. Red lines indicate the edges of the in-plane Brillouin zone. (b) Energy-momentum ARPES intensity map around the bulk Γ_{002} point along the in-plane $k_{\langle 11\bar{2}0\rangle}$ direction, measured at $h\nu = 25$ eV with linear-horizontal light polarization. The red curve is the momentum distribution curve over $E_F \pm 5$ meV. The black vertical bars show the Fermi momenta k_F^i and k_F^o of the inner and outer subbands, respectively. The Fermi liquid is coupled to phonons with a characteristic Debye energy ω_D shown by the horizontal, dashed black line. Photoemission data in this and all other figures of this paper were measured at $T = 7$ K.

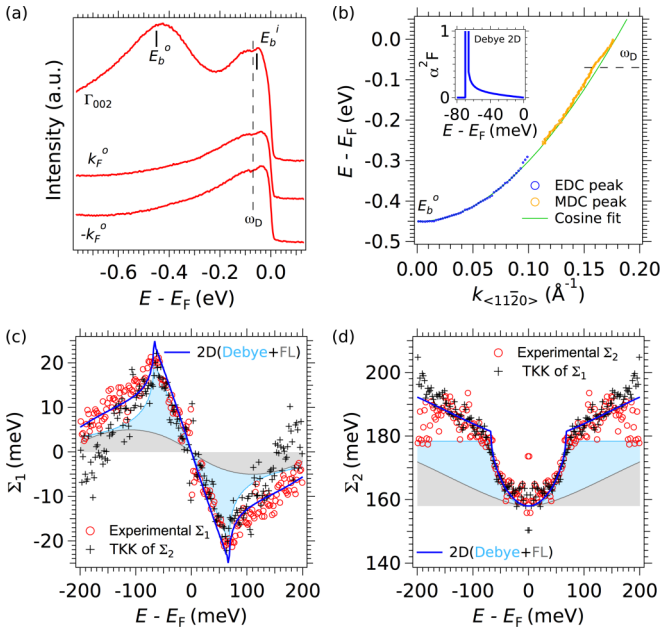

FIG. 3. (a) EDCs of the ARPES dispersion map, Fig. 2(b), respectively over $\Gamma \pm 0.05$ Å^{-1} (upper curve) and $\pm k_F^o \pm 0.05$ Å^{-1} (mid and lower curve). The peaks near E_F for both the inner and outer subbands show a peak-dip-hump structure, with the dip at an energy $\omega_D = -70$ meV. (b) Maxima of the EDC (blue circles) and MDC (orange circles) peaks for the outer subband of the 2DES the Al(2 Å)/ZnO(000$\bar{1}$) interface. Only data for the right branch ($k > 0$) are shown. The continuous green curve is a cosine fit to the data representing the noninteracting electron dispersion of this subband. (c), (d) Experimental real and imaginary parts of the electron self-energy (red circles), and their Kramers–Kronig transforms (black crosses), for the right branch of the outer subband. The dark blue curves are simultaneous fits to Σ_1 and Σ_2 using a 2D Fermi-liquid + Debye model. The 2D Fermi-liquid and 2D Debye components of the fit are shown by the filled light blue and gray curves. Data were symmetrized with respect to E_F, as required by Kramers–Kronig. Similar results are obtained by an analysis of the left branch of the outer subband (see supplementary material [45]). The inset in panel (b) shows the Eliashberg coupling function resulting from the 2D Debye model used.

The subbands' Fermi momenta, determined from the maxima of the momentum distribution curve (MDC) integrated over $E_F \pm 5$ meV [see red curve at top of Fig. 2(b)], are $k_F^o = (0.17 \pm 0.005)$ Å^{-1} and $k_F^i = (0.07 \pm 0.005)$ Å^{-1}. Their band bottoms, extracted from the maxima of the energy distribution curve (EDC) over $\Gamma \pm 0.05$ Å^{-1} and the dispersion of the EDC peaks [Figs. 3(a) and 3(b)], are located at binding energies $E_b^o = (450 \pm 5)$ meV and $E_b^i = (55 \pm 5)$ meV. Due to the light and isotropic band mass of the s-type electrons forming the 2DES, the subband splitting in ZnO is ≈3 times larger than in titanates [32]. The thickness of the 2DES can be estimated from the subbands' binding energies and energy separation by assuming a triangular-wedge quantum well, yielding 21 Å (or four unit cells) along c (see supplemental material [45] for details).

From the area enclosed by the in-plane Fermi circles (A_F), the density of electrons in the 2DES is $n_{2D} = A_F/(2\pi^2) = (5.4 \pm 0.3) \times 10^{13}$ cm^{-2}, or about 0.14 electrons per hexagonal unit cell in the (000$\bar{1}$) plane. Such electron density is far larger than the critical value, estimated at 3.8×10^{12} cm^{-2}, at which the crossover from a polaronic to a Fermi liquid regime for electron-phonon coupling occurs [44].

The effective masses around Γ of the outer and inner subbands, determined from their Fermi momenta and band bottoms using free-electron parabola approximations, are respectively $m_o^\star = (0.25 \pm 0.02)m_e$ and $m_i^\star = (0.34 \pm 0.08)m_e$, where m_e is the free-electron mass. The mass of the outer subband agrees well with the conduction-band mass along the (000$\bar{1}$) plane calculated for bulk stoichiometric ZnO or determined from infrared reflectivity and cyclotron resonance experiments on lightly doped ZnO [1,2].

Importantly, note that the circular form of the Fermi surfaces, Fig. 2(a), implies that band-structure anisotropies, nonparabolicity, and warping are negligible for the observed band filling. Thus, the different masses of the two subbands cannot be assigned to such effects.

As the confinement of noninteracting electrons in a quantum well should result in subbands with the same effective mass, we focus on analyzing the renormalization of the inner band in the following paragraphs.

In fact, as seen from Figs. 2(b) and 3(a), the band bottom of the *inner* subband presents a complex structure, with a peak-dip-hump clearly seen in the EDC around Γ. Likewise, as shown in Figs. 2(b), 3(a) and 3(b), the *outer* subband shows a *kink* in its dispersion at approximately the same binding energy ($\omega_D = 70$ meV) of the dip observed in the inner band, together with a peak-dip-hump for the EDCs around its Fermi momenta. As will be shown shortly, all these features result from electron-phonon coupling.

The quantification of the electron-phonon interaction is possible through the analysis of the energy-dependent real (Σ_1)

and imaginary (Σ_2) parts of the electron self-energy. These can be inferred from the spectral function of the many-electron system, directly measured by ARPES [55]. Thus, we extract and model the self-energy of the outer band, and then use the results to renormalize the inner band, which is difficult to fit due to the peak-dip-hump structure.

Figure 3(b) shows the dispersion of the spectral function peak for the outer subband, extracted from the maxima of the EDCs (blue circles) and MDCs (orange circles). The continuous green line is a cosine fit to the data representing the bare (i.e., noninteracting) electron dispersion of this subband. The energy difference between the MDC peak and the bare band gives the real part of the electron self-energy and is plotted in Fig. 3(c), red circles. The pronounced *peak* in Σ_1 at $E - E_F \approx -70$ meV corresponds to the kink in the experimental dispersion. Likewise, the energy dependence of the MDCs linewidths gives the imaginary part of the electron self-energy (or electronic scattering rate) and is shown in Fig. 3(d), red circles. Here, one observes a rapid increase of the scattering rate from E_F down to the binding energy at which the real part of the self-energy peaks, followed by a less rapid but steady increase. To check the consistency of the self-energy extracted from our data, we compute the Kramers–Kronig transformation (TKK) of the experimental $\Sigma_2(E)$ [respectively $\Sigma_1(E)$], black crosses in Fig. 3(c) [respectively Fig. 3(d)]. We observe an excellent agreement between $\Sigma_1(E)$ and TKK$\{\Sigma_2(E)\}$ [respectively between $\Sigma_2(E)$ and TKK$\{\Sigma_1(E)\}$], ensuring that our analysis and choice of bare dispersion respect causality.

The simultaneous occurrence of a pronounced peak in Σ_1 and an abrupt change in slope in Σ_2 at about the same energy ω_D, as observed in Figs. 3(c) and 3(d), are typical landmarks of the interaction between the electron liquid and some collective modes of the solid (e.g., phonons) having a characteristic energy ω_D [55]. Thus, we fit the experimental complex self-energy with a model of a Fermi liquid with Debye electron-phonon coupling, both in 2D [56,57], as shown by the continuous blue curves in Figs. 3(c) and 3(d). The fit gives a Debye frequency of 68 ± 2 meV, in excellent agreement with our data and the phonon energies (up to about 580 cm^{-1}, or ≈70 meV) measured by other techniques [1,6], and a dimensionless coupling constant $\lambda = 0.3 \pm 0.05$. The isotropic Fermi liquid of the fit is characterized by a carrier density of $(6.7 \pm 0.4) \times 10^{13}$ cm^{-2}, close to the experimental value. The electron-phonon, or Eliashberg, coupling function $\alpha^2 F(\omega)$ resulting from the 2D Debye model used is shown in the inset of Fig. 3(b). We checked that a fit with a three-dimensional (3D) Fermi-liquid + Debye model [56,58] yields a larger phonon cutoff energy, of the order of 85 meV, and an overall poor agreement with the experimental self-energy. The details of the models and a comparison of the obtained fits are given in the supplemental material [45].

We now turn to the inner subband. To model it, we rigidly shift the bare outer band in energy and then renormalize it using the previously deduced self-energy. As shown by the red curve in Fig. 4(a), a shift of 377 meV fits the experimental Fermi momenta, matching the required conservation of the 2D electron density. The resulting renormalized inner band [the black curve in Fig. 4(a)] compares excellently with the experimental inner band.

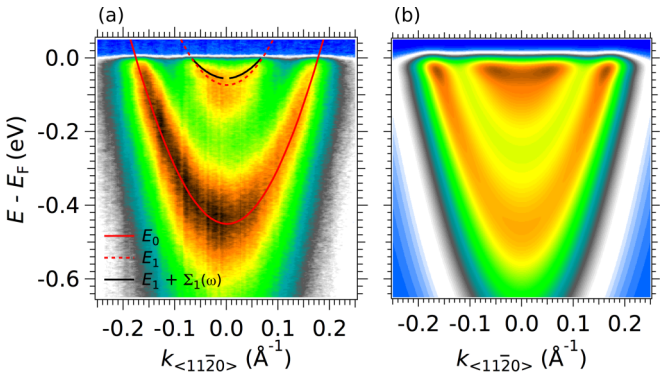

FIG. 4. (a) Zoom over the energy-momentum ARPES map of Fig. 2(b). The continuous red curve is the cosine fit to the bare outer subband. The dashed red curve is the same fit up-shifted by 377 meV, until it matches the Fermi momenta of the inner subband, representing thus the bare inner subband. The black curve is the *renormalized* inner subband, obtained by adding the experimental Σ_1 extracted from the *outer* subband, Fig. 3(c), to the bare *inner* subband. (b) Simulation of the ARPES data, using the self-energy of the 2D Fermi-liquid + Debye model fit to the data plus a constant electronic scattering rate of approximately 160 meV, corresponding to Σ_2 at E_F from Fig. 3(d). The calculated spectral function was multiplied by the Fermi–Dirac distribution and then convoluted with a Gaussian resolution function of FWHM = 20 meV.

To cross-check the above analysis of the ARPES data, we simulated the whole 2DES spectral function using the self-energy of the 2D Fermi-liquid + Debye model fit to the data. The resulting ARPES map [Fig. 4(b)] compares well with the data. Thus, the *entire* electronic structure of the 2DES at the Al(2 Å)/ZnO(000$\bar{1}$) surface can be understood from doping of the bulk conduction band by oxygen vacancies, electron confinement due to band-bending induced by those vacancies, and coupling of the ensuing subbands with a Debye-like distribution of phonons.

Note that, in the present case of a high carrier density, the coupling constant λ gives directly the electron mass renormalization $m^\star$ due to electron-phonon interaction; namely, $m^\star/m_0 = 1 + \lambda$ [59], where m_0 is the noninteracting band mass. Using parabolic approximations (i.e., energy-independent band masses) for the subbands' dispersions, we can assume that the bottom of the outer band, located well below the phonon energies, gives the noninteracting band mass, while the inner band, located just above the Debye energy, gives the electron mass fully renormalized by coupling to phonons. This yields a coupling constant $\lambda \approx 1 - m_i^\star/m_o^\star = 0.36 \pm 0.3$, subject to large errors, but in overall agreement with the more accurate value obtained above from the fit to the whole energy-dependent complex self-energy.

More generally, in insulating dielectric oxides, the electron-phonon coupling can significantly depend on the electron density, due to different screening mechanism of the oscillating ions. At low densities (i.e., band fillings smaller or comparable to the phonon cutoff frequency), screening based on dielectric polarization results in large, spatially delocalized, polarons. At high densities the increased electronic screening of the ionic lattice vibrations result in a Fermi-liquid regime with weaker electron phonon coupling [44]. Those two regimes

were recently characterized by ARPES in anatase-TiO_2(001) [41] and $SrTiO_3$ [42]. Note furthermore that the electron-phonon coupling constant $\lambda = 0.3$ obtained here is significantly smaller than the coupling constant observed in the Fermi-liquid regime of anatase-TiO_2 and $SrTiO_3$ ($\lambda_{FL}^{TiO_2} \approx \lambda_{FL}^{SrTiO_3} = 0.7$) [41,42,60]. This suggests that, in the high-carrier-density regime, the electronic screening for electron-phonon coupling is more efficient for the *s* electrons of the 2DESs in ZnO than for the *d* electrons of the 2DESs in TMOs.

Notably, our self-consistent Kramers–Kronig analysis of the self-energy in ZnO, and the deduction of the electron-phonon coupling parameter using a Debye model, is different from previous approaches used in other oxides, like $SrTiO_3$ [61], where λ was inferred from the slope of Σ_1 at E_F (i.e., the renormalization of quasiparticle mass), or TiO_2 anatase, where it was estimated by modeling the self-energy to reproduce the data [41]. Note that the coupling parameters deduced from the renormalization of quasiparticle mass, velocity, and spectral weight in ARPES data are in general subject to large errors, as mentioned before, and distinct from the true microscopic coupling parameter [62].

As a whole, our results highlight the universal character of the approach based on surface redox reactions to create 2DESs in functional oxides [31], unveil similarities and differences between *s*- and *d*-orbital-type 2DES, and add new ingredients to the rich many-body physics displayed by confined electronic states in ZnO. Our observations suggest that oxygen vacancies can contribute to electron-doping near the surface of ZnO, motivating further experimental and theoretical studies on the formation and role of vacancies at surfaces and interfaces of this important transparent semiconductor oxide. Moreover, the realization of a highly doped 2DES in ZnO opens a new realm of possibilities, such as high-power applications using a transparent oxide semiconductor that presents many advantages with respect to standard Sn-doped In_2O_3 (ITO): ZnO is more abundant, cheaper, easier to fabricate and process, nontoxic, and when doped it can attain mobilities comparable to those of ITO [1–3].

We thank S. Sengupta and M. Monteverde for discussions. Work at CSNSM was supported by public grants from the French National Research Agency (ANR), project LACUNES No. ANR-13-BS04-0006-01, and the "Laboratoire d'Excellence Physique Atomes Lumière Matière" (LabEx PALM projects ELECTROX and 2DEG2USE) overseen by the ANR as part of the "Investissements d'Avenir" program (reference: ANR-10-LABX-0039). Work at KEK-PF was supported by Grants-in-Aid for Scientific Research (Grants No. 16H02115 and No. 16KK0107) from the Japan Society for the Promotion of Science (JSPS). Experiments at KEK-PF were performed under the approval of the Program Advisory Committee (Proposals 2016G621 and 2015S2005) at the Institute of Materials Structure Science at KEK. T.C.R. acknowledges funding from the RTRA–Triangle de la Physique (project PEGASOS). A.F.S.-S. thanks support from the Institut Universitaire de France.

T.C.R. and J.D. contributed equally to this work.

[1] C. F. Klingshirn, B. K. Meyer, A. Waag, A. Hoffmann, and J. Geurts, *Zinc Oxide: From Fundamental Properties Towards Novel Applications*, Springer Series in Materials Science, Vol. 120 (Springer-Verlag, Berlin and Heidelberg, 2010).

[2] H. Morkoaąnd and Ü. Özgür, *Zinc Oxide: Fundamentals, Materials and Device Technology* (Wiley-VCH Verlag GmbH & Co. KGaA, Weinheim, 2009).

[3] M. Lorenz *et al.*, The 2016 oxide electronic materials and oxide interfaces roadmap, J. Phys. D **49**, 433001 (2016).

[4] X. Y. Liu, C. X. Shan, H. Zhu, B. H. Li, M. M. Jiang, S. F. Yu, and D. Z. Shen, Ultraviolet lasers realized via electrostatic doping method, Sci. Rep. **5**, 13641 (2015).

[5] A. Bakin, A. El-Shaer, A. C. Mofor, M. Al-Suleiman, E. Schlenker, and A. Waag, ZnMgO-ZnO quantum wells embedded in ZnO nanopillars: Towards realization of nano-LEDS, Phys. Status Solidi C **4**, 158 (2007).

[6] Ü. Özgur, Ya. I. Alivov, C. Liu, A. Teke, M. A. Reshchikov, S. Doan, V. Avrutin, S.-J. Cho, and H. Morko, A comprehensive review of ZnO materials and devices, J. Appl. Phys. **98**, 041301 (2005).

[7] Y. Tokura, Orbital physics in transition-metal oxides, Science **288**, 462 (2000).

[8] E. Dagotto, Complexity in strongly correlated electronic systems, Science **309**, 257 (2005).

[9] A. Tsukazaki, A. Ohtomo, T. Kita, Y. Ohno, H. Ohno, and M. Kawasaki, Quantum Hall effect in polar oxide heterostructures, Science **315**, 1388 (2007).

[10] A. Tsukazaki, S. Akasaka, K. Nakahara, Y. Ohno, H. Ohno, D. Maryenko, A. Ohtomo, and M. Kawasaki, Observation of the fractional quantum Hall effect in an oxide, Nat. Mater. **9**, 889 (2010).

[11] A. Ohtomo and H. Y. Hwang, A high-mobility electron gas at the $LaAlO_3/SrTiO_3$ heterointerface, Nature (London) **427**, 423 (2004).

[12] S. Thiel, G. Hammerl, A. Schmehl, C. W. Schneider, and J. Mannhart, Tunable quasi-two-dimensional electron gases in oxide heterostructures, Science **313**, 1942 (2006).

[13] N. Reyren, S. Thiel, A. D. Caviglia, L. Fitting Kourkoutis, G. Hammerl, C. Richter, C. W. Schneider, T. Kopp, A.-S. Rüetschi, D. Jaccard, M. Gabay, D. A. Muller, J.-M. Triscone, and J. Mannhart, Superconducting interfaces between insulating oxides, Science **317**, 1196 (2007).

[14] K. Ueno, S. Nakamura, H. Shimotani, A. Ohtomo, N. Kimura, T. Nojima, H. Aoki, Y. Iwasa, and M. Kawasaki, Electric-field-induced superconductivity in an insulator, Nat. Mater. **7**, 855 (2008).

[15] A. Brinkman, M. Huijben, M. van Zalk, J. Huijben, U. Zeitler, J. C. Maan, W. G. van der Wiel, G. Rijnders, D. H. A. Blank, and H. Hilgenkamp, Magnetic effects at the interface between non-magnetic oxides, Nat. Mater. **6**, 493 (2007).

[16] A. D. Caviglia, S. Gariglio, N. Reyren, D. Jaccard, T. Schneider, M. Gabay, S. Thiel, G. Hammerl, J. Mannhart, and J.-M. Triscone, Electric field control of the $LaAlO_3/SrTiO_3$ interface ground state, Nature (London) **456**, 624 (2008).

[17] A. D. Caviglia, M. Gabay, S. Gariglio, N. Reyren, C. Cancellieri, and J. M. Triscone, Tunable Rashba Spin-Orbit Interaction at Oxide Interfaces, Phys. Rev. Lett. **104**, 126803 (2010).

[18] A. Joshua, J. Ruhman, S. Pecker, E. Altman, and S. Ilani, Gate-tunable polarized phase of two- dimensional electrons at the LaAlO3/SrTiO3 interface, Proc. Natl. Acad. Sci. USA **110**, 9633 (2013).

[19] Y. Z. Chen, N. Bovet, F. Trier, D. V. Christensen, F. M. Qu, N. H. Andersen, T. Kasama, W. Zhang, R. Giraud, J. Dufouleur, T. S. Jespersen, J. R. Sun, A. Smith, J. Nygård, L. Lu, B. Büchner, B. G. Shen, S. Linderoth, and N. Pryds, A high-mobility two-dimensional electron gas at the spinel/perovskite interface of c-Al_2O_3/$SrTiO_3$, Nat. Commun. **4**, 1371 (2013).

[20] Y. Z. Chen, F. Trier, T. Wijnands, R. J. Green, N. Gauquelin, R. Egoavil, D. V. Christensen, G. Koster, M. Huijben, N. Bovet, S. Macke, F. He, R. Sutarto, N. H. Andersen, J. A. Sulpizio, M. Honig, G. E. D. K. Prawiroatmodjo, T. S. Jespersen, S. Linderoth, S. Ilani, J. Verbeeck, G. Van Tendeloo, G. Rijnders, G. A. Sawatzky, and N. Pryds, Extreme mobility enhancement of two-dimensional electron gases at oxide interfaces by charge-transfer-induced modulation doping, Nat. Mater. **14**, 801 (2015).

[21] T. D. Ngo, J.-W. Chang, K. Lee, S. Han, J. S. Lee, Y. H. Kim, M.-H. Jung, Y.-J. Doh, M.-S. Choi, J. Song, and J. Kim, Polarity-tunable magnetic tunnel junctions based on ferromagnetism at oxide heterointerfaces, Nat. Commun. **6**, 8035 (2015).

[22] D. Stornaiuolo, C. Cantoni, G. M. De Luca, R. Di Capua, E. Di. Gennaro, G. Ghiringhelli, B. Jouault, D. Marrè, D. Massarotti, F. Miletto Granozio, I. Pallecchi, C. Piamonteze, S. Rusponi, F. Tafuri, and M. Salluzzo, Tunable spin polarization and superconductivity in engineered oxide interfaces, Nat. Mater. **15**, 278 (2016).

[23] A. F. Santander-Syro, O. Copie, T. Kondo, F. Fortuna, S. Pailhès, R. Weht, X. G. Qiu, F. Bertran, A. Nicolaou, A. Taleb-Ibrahimi, P. Le Fèvre, G. Herranz, M. Bibes, N. Reyren, Y. Apertet, P. Lecoeur, A. Barthélémy, and M. J. Rozenberg, Two-dimensional electron gas with universal subbands at the surface of $SrTiO_3$, Nature (London) **469**, 189 (2011).

[24] W. Meevasana, P. D. C. King, R. H. He, S.-K. Mo, M. Hashimoto, A. Tamai, P. Songsiriritthigul, F. Baumberger, and Z.-X. Shen, Creation and control of a two-dimensional electron liquid at the bare $SrTiO_3$ surface, Nat. Mater. **10**, 114 (2011).

[25] A. F. Santander-Syro, C. Bareille, F. Fortuna, O. Copie, M. Gabay, F. Bertran, A. Taleb-Ibrahimi, P. Le Fèvre, G. Herranz, N. Reyren, M. Bibes, A. Barthélémy, P. Lecoeur, J. Guevara, and M. J. Rozenberg, Orbital symmetry reconstruction and strong mass renormalization in the two-dimensional electron gas at the surface of $KTaO_3$, Phys. Rev. B **86**, 121107(R) (2012).

[26] P. D. C. King, R. H. He, T. Eknapakul, P. Buaphet, S.-K. Mo, Y. Kaneko, S. Harashima, Y. Hikita, M. S. Bahramy, C. Bell, Z. Hussain, Y. Tokura, Z.-X. Shen, H. Y. Hwang, F. Baumberger, and W. Meevasana, Subband Structure of a Two-Dimensional Electron Gas formed at the Polar Surface of the Strong Spin-Orbit Perovskite $KTaO_3$, Phys. Rev. Lett. **108**, 117602 (2012).

[27] C. Bareille, F. Fortuna, T. C. Rödel, F. Bertran, M. Gabay, O. Hijano Cubelos, A. Taleb-Ibrahimi, P. Le Fèvre, M. Bibes, A. Barthélémy, T. Maroutian, P. Lecoeur, M. J. Rozenberg, and A. F. Santander-Syro, Two-dimensional electron gas with six-fold symmetry at the (111) surface of $KTaO_3$, Sci. Rep. **4**, 3586 (2014).

[28] T. C. Rödel, C. Bareille, F. Fortuna, C. Baumier, F. Bertran, P. Le Fèvre, M. Gabay, O. Hijano Cubelos, M. J. Rozenberg, T. Maroutian, P. Lecoeur, and A. F. Santander-Syro, Orientational tuning of the Fermi sea of confined electrons at the $SrTiO_3$(110) and (111) surfaces, Phys. Rev. Appl. **1**, 051002 (2014).

[29] S. McKeown Walker, A. de la Torre, F. Y. Bruno, A. Tamai, T. K. Kim, M. Hoesch, M. Shi, M. S. Bahramy, P. D. C. King, and F. Baumberger, Control of a Two-Dimensional Electron Gas on $SrTiO_3$(111) by Atomic Oxygen, Phys. Rev. Lett. **113**, 177601 (2014).

[30] T. C. Rödel, F. Fortuna, F. Bertran, M. Gabay, M. J. Rozenberg, A. F. Santander-Syro, and P. Le Fèvre, Engineering of two-dimensional electron gases at the (001) and (101) surfaces of TiO_2 anatase using light, Phys. Rev. B **92**, 041106(R) (2015).

[31] T. C. Rödel, F. Fortuna, S. Sengupta, E. Frantzeskakis, P. Le Fèvre, F. Bertran, B. Mercey, S. Matzen, G. Agnus, T. Maroutian, P. Lecoeur, and A. F. Santander-Syro, Universal fabrication of 2D electron systems in functional oxides, Adv. Mater. **28**, 1976 (2016).

[32] T. C. Rödel, M. Vivek, F. Fortuna, P. Le Fèvre, F. Bertran, R. Weht, J. Goniakowski, M. Gabay, and A. F. Santander-Syro, Two-dimensional electron systems in $ATiO_3$ perovskites (A = Ca, Ba, Sr): Control of orbital hybridization and energy order, Phys. Rev. B **96**, 041121(R) (2017).

[33] E. Frantzeskakis, T. C. Rödel, F. Fortuna, and A. F. Santander-Syro, 2D surprises at the surface of 3D materials: Confined electron systems in transition metal oxides, J. Electron Spectrosc. Relat. Phenom. **219**, 16 (2017).

[34] T. Taniuchi, Y. Motoyui, K. Morozumi, T. C. Rödel, F. Fortuna, A. F. Santander-Syro, and S. Shin, Imaging of room-temperature ferromagnetic nano-domains at the surface of a non-magnetic oxide, Nat. Commun. **7**, 11781 (2016).

[35] R. A. Powell, W. E. Spicer, and J. C. McMenamin, Photoemission studies of wurtzite zinc oxide, Phys. Rev. B **6**, 3056 (1972).

[36] W. Göpel, J. Pollmann, I. Ivanov, and B. Reihl, Angle-resolved photoemission from polar and non-polar zinc oxide surfaces, Phys. Rev. B **26**, 3144 (1982).

[37] K. Ozawa, K. Sawada, Y. Shirotori, and K. Edamoto, Angle-resolved photoemission study of the valence band structure of ZnO(10$\bar{1}$0), J. Phys.: Condens. Matter **17**, 1271 (2005).

[38] K. Ozawa and K. Mase, Metallization of ZnO(10$\bar{1}$0) by adsorption of hydrogen, methanol, and water: Angle-resolved photoelectron spectroscopy, Phys. Rev. B **81**, 205322 (2010).

[39] L. F. J. Piper, A. R. H. Preston, A. Fedorov, S. W. Cho, A. DeMasi, and K. E. Smith, Direct evidence of metallicity at ZnO(000$\bar{1}$)-(1 × 1) surfaces from angle-resolved photoemission spectroscopy, Phys. Rev. B **81**, 233305 (2010).

[40] J.-C. Deinert, O. T. Hofmann, M. Meyer, P. Rinke, and J. Stähler, Local aspects of hydrogen-induced metallization of the ZnO(10$\bar{1}$0) surface, Phys. Rev. B **91**, 235313 (2015).

[41] S. Moser, L. Moreschini, J. Jaćimović, O. S. Barišić, H. Berger, A. Magrez, Y. J. Chang, K. S. Kim, A. Bostwick, E. Rotenberg, L. Forró, and M. Grioni, Tunable Polaronic Conduction in Anatase TiO_2, Phys. Rev. Lett. **110**, 196403 (2013).

[42] Z. Wang, S. McKeown Walker, A. Tamai, Y. Wang, Z. Ristic, F. Y. Bruno, A. de la Torre, S. Ricco, N. C. Plumb, M. Shi, P. Hlawenka, J. Sanchez-Barriga, A. Varykhalov, T. K. Kim, M. Hoesch, P. D. C. King, W. Meevasana, U. Diebold, J. Mesot, B. Moritz, T. P. Devereaux, M. Radovic, and F. Baumberger, Tailoring the nature and strength of electron-phonon interactions

in the SrTiO3(001) 2D electron liquid, Nat. Mater. **15**, 835 (2016).

[43] R. Yukawa, K. Ozawa, S. Yamamoto, H. Iwasawa, K. Shimada, E. F. Schwier, K. Yoshimatsu, H. Kumigashira, H. Namatame, M. Taniguchi, and I. Matsuda, Phonon-dressed two-dimensional carriers on the ZnO surface, Phys. Rev. B **94**, 165313 (2016).

[44] C. Verdi, F. Caruso, and F. Giustino, Origin of the crossover from polarons to Fermi liquids in transition metal oxides, Nat. Commun. **8**, 15769 (2017).

[45] See supplementary material at http://link.aps.org/supplemental/10.1103/PhysRevMaterials.2.051601 for further details about the ZnO crystal structure and notations, surface preparation, aluminum deposition, ARPES measurements, confinement potential, fitting of the data using the Debye and Fermi-liquid models of the self-energy, and the 2DES at the Zn-terminated surface.

[46] S. Backes, T. C. Rödel, F. Fortuna, E. Frantzeskakis, P. Le Fèvre, F. Bertran, M. Kobayashi, R. Yukawa, T. Mitsuhashi, M. Kitamura, K. Horiba, H. Kumigashira, R. Saint-Martin, A. Fouchet, B. Berini, Y. Dumont, A. J. Kim, F. Lechermann, H. O. Jeschke, M. J. Rozenberg, R. Valentí, and A. F. Santander-Syro, Hubbard band versus oxygen vacancy states in the correlated electron metal $SrVO_3$, Phys. Rev. B **94**, 241110(R) (2016).

[47] S. McKeown Walker, F. Y. Bruno, Z. Wang, A. de la Torre, S. Riccó, A. Tamai, T. K. Kim, M. Hoesch, M. Shi, M. S. Bahramy, P. D. C. King, and F. Baumberger, Carrier-density control of the $SrTiO_3$(001) surface 2D electron gas studied by ARPES, Adv. Mater. **27**, 3894 (2015).

[48] S. Tanaka, K. Mase, and S. Nagaoka, Photostimulated ion desorption from the TiO_2 (110) and ZnO surfaces, Surf. Sci. **572**, 43 (2004).

[49] A. Janotti and C. G. Van de Walle, Oxygen vacancies in ZnO, Appl. Phys. Lett. **87**, 122102 (2005).

[50] A. Janotti and C. G. Van de Walle, Hydrogen multicentre bonds, Nat. Mater. **6**, 44 (2007).

[51] A. Janotti and C. G. Van de Walle, Fundamentals of zinc oxide as a semiconductor, Rep. Prog. Phys. **72**, 126501 (2009).

[52] S. Lany and A. Zunger, Many-body GW calculation of the oxygen vacancy in ZnO, Phys. Rev. B **81**, 113201 (2010).

[53] Y.-S. Kim and C. H. Park, Rich Variety of Defects in ZnO via an Attractive Interaction between O Vacancies and Zn Interstitials: Origin of n-Type Doping, Phys. Rev. Lett. **102**, 086403 (2009).

[54] R. Gurwitz, R. Cohen, and I. Shalisha, Interaction of light with the ZnO surface: Photon induced oxygen breathing, oxygen vacancies, persistent photoconductivity, and persistent photovoltage, J. Appl. Phys. **115**, 033701 (2014).

[55] S. Hüfner, *Photoelectron Spectroscopy: Principles and Applications*, 3rd ed. (Springer, Berlin, 2003).

[56] G. F. Giuliani and G. Vignale, *Quantum Theory of the Electron Liquid* (Cambridge University Press, 2005).

[57] V. N. Kostur and B. Mitrović, Electron-phonon interaction in two dimensions: Variations of $\mathrm{Im}\Sigma(\epsilon_p,\omega)$ with increasing ω_D/E_F, Phys. Rev. B **48**, 16388 (1993).

[58] S. Engelsberg and J. Schrieffer, Coupled electron-phonon system, Phys. Rev. **131**, 993 (1963).

[59] F. Giustino, Electron-phonon interactions from first principles, Rev. Mod. Phys. **89**, 015003 (2017).

[60] W. Meevasana, X. J. Zhou, B. Moritz, C.-C. Chen, R. H. He, S.-I. Fujimori, D. H. Lu, S.-K. Mo, R. G. Moore, F. Baumberger, T. P. Devereaux, D. van der Marel, N. Nagaosa, J. Zaanen, and Z.-X. Shen, Strong energy-momentum dispersion of phonon-dressed carriers in the lightly doped band insulator $SrTiO_3$, New J. Phys. **12**, 023004 (2010).

[61] P. D. C. King, S. McKeown Walker, A. Tamai, A. de la Torre, T. Eknapakul, P. Buaphet, S.-K. Mo, W. Meevasana, M. S. Bahramy, and F. Baumberger, Quasiparticle dynamics and spin-orbital texture of the $SrTiO_3$ two-dimensional electron gas, Nat. Commun. **5**, 3414 (2014).

[62] C. N. Veenstra, G. L. Goodvin, M. Berciu, and A. Damascelli, Elusive electron-phonon coupling in quantitative analyses of the spectral function, Phys. Rev. B **82**, 012504 (2010).